PHYSICAL REVIEW B VOLUME 46, NUMBER 18 1 NOVEMBER 1992-II

Oxide-growth kinetics and fractal-like patterning across liquid gallium surfaces

Jan M. Chabala
The Enrico Fermi Institute and Department of Physics, The University of Chicago, 5640 South Ellis Avenue, Chicago, Illinois 60637

(Received 2 April 1992; revised manuscript received 16 July 1992)

Gallium oxide initially forms fractal-like structures as it grows laterally across bounded clean surfaces of liquid gallium. The growing oxide film is no more than a few monolayers thick. During later growth, the oxide perimeter becomes rounded and uniform gaps develop between neighboring growth fronts. The measured fractal dimension of the oxide patterns increases from less than 1.6 to 2.0. In this experiment, the oxide is constrained to grow over liquid surfaces $\leq (80\ \mu m)^2$. To good approximation, for fixed growth time, liquid temperature, and ambient oxygen pressure, the fractional oxide coverage is independent of the area enclosed by the original boundary. The liquid area decreases exponentially with time as it is blanketed by the oxide film. These results suggest that the oxidation is the result of an irreversible nonequilibrium diffusion aggregation process across the liquid surface, modified by the action of (undetected) impurities on the interface between the oxide and clean liquid. The change in oxide coverage is modeled as a function of time, liquid temperature, ambient oxygen pressure, and area of the original enclosing boundary. The data were acquired using imaging secondary-ion mass spectrometry, with a spatial resolution of 100 nm.

I. INTRODUCTION

The oxidation of metal surfaces has been extensively studied for decades. Recent comprehensive reviews outline the progress of this research.[1,2] Given this large body of work, it is remarkable that oxidation on liquid metal surfaces has received little attention. This dearth of research is due, in large part, to the difficulty of applying traditional metallurgical techniques (such as those using electron or x-ray probes) to liquid samples in an ultrahigh vacuum environment (to halt oxidation within the analytical instrument). The ubiquity of oxygen affects many surface properties and reactions. Frequently, oxygen complicates surface analyses and its presence is treated as a nuisance.

Numerous questions concerning the initial stages of oxidation on liquid metals remain unanswered. Oxygen adsorption and mobility over the liquid surface, nucleation, and lateral growth of the oxide phase, and the effect of impurities are not well understood. Information derived from the study of liquids may be applicable to problems in solid material research. For example, oxide distributions formed over the melt may be imprinted onto a metal as it is solidified, affecting the future properties of the solid. A few groups have used nonimaging analytical techniques to study oxidation on liquid metals.[3] It is interesting to explore the lateral development of oxide across surfaces, in order to correlate the oxide growth with localized features such as impurities and fixed (or floating) solid structures. This research is further motivated by the chemical similarity between gallium and aluminum. Additional studies, grounded on the present work and employing the techniques described here, should lead to a better understanding of the corrosion and oxidation of this pervasive metal.

Gallium is a convenient metal for liquid oxidation studies because it has a low melting temperature (29.8 °C), has a strong tendency to supercool, and is liquid over a wide temperature range. Moreover, because it has a very low vapor pressure[4] ($<10^{-11}$ Torr), its surface can be cleaned within an ultrahigh vacuum analytical instrument and the ambient oxygen pressure can be reduced sufficiently to effectively stop the formation of oxide (β-Ga_2O_3).[5] This phase forms readily with a significant heat of formation (-258 K cal/g mole at 25 °C). However, because there is a large change in ordering between the oxygen-on-liquid and gallium oxide phases, an activation energy (E_A) barrier may limit the rate of oxide formation.

Imaging secondary ion-mass spectrometry (SIMS) was used to analyze the lateral distribution of the oxide during growth.[6,7] These measurements were performed with a high-spatial-resolution scanning ion microprobe (SIM) employing a tightly focused Ga^+ primary ion beam. For this experiment, the spatial resolving power of the instrument was ~100 nm. The base pressure in the analytical chamber was 2×10^{-9} Torr, low enough to stop oxidation.[5] The gallium oxide growth was confined to sputter-cleaned liquid regions of finite area, $\leq(80\ \mu m)^2$. This growth area, or "window," is bounded by the unremoved oxide covering adjacent liquid.

The formation of the oxide over these clean windows was studied for several different window areas, ambient O_2 pressures, and liquid temperatures. The time evolution of the oxide distributions under these conditions was monitored *in situ* by acquiring SIMS images after increasing growth periods. The resulting images were analyzed for oxide coverage, perimeter, fractal dimension, and (qualitatively) oxide thickness. The fractional oxide coverage (coverage normalized to the area of the original boundary window) and uncovered liquid area are easily derived from these data.

We find that, initially, fractal-like oxide structures form that can be understood within a simple nonequilibrium diffusion limited aggregation (DLA) picture. Later, the oxide evolves into smooth-boundary patterns separated by uniform gaps of unoxidized liquid. The measured dimension of this late-growth oxide approaches 2.0. We successfully model the observed oxidation kinetics as a function of time, liquid temperature, ambient oxygen pressure, and original window area. Finally, we propose several mechanisms that may be responsible for the distinguishing features observed during later growth. Key to these proposals is the introduction of an effective interface tension, and possibly oxide reordering, along the growth front. These additional phenomena are consequences of the presence of impurities on the liquid.

II. EXPERIMENTAL

A. Analytical instrument and the secondary ion-mass spectrometry technique

The experiment was performed with the University of Chicago Scanning Ion Microprobe (SIM), which has been described in detail elsewhere.[8,9] This instrument utilizes a 30-pA, 40-keV Ga^+ primary ion beam focused to a spot 50 nm in diameter (full width half maximum). Because of statistical considerations,[10] the effective spatial resolution is ~100 nm for the experimental configuration of this study. The primary beam is composed of the same material as the liquid studied (with the same purity), minimizing sample contamination.

The scanned beam is used both to sputter-clean surfaces and to obtain analytical information by imaging secondary ion-mass spectrometry (SIMS). In the latter mode, secondary ions emitted by sputtering are separated according to their mass-to-charge ratio with an RF quadrupole mass spectrometer. These secondary ions originate from, and consequently carry information about, the most superficial 1–3 monolayers of the sample.[11,12] Ions filtered through the spectrometer are detected individually with a channel electron multiplier. SIMS images are generated by tuning the system to transmit and detect a single secondary ion species while the probe is scanned over a square region of the surface. The resulting signal, correlated with the scan position on the surface, is recorded in arrays of digital memory for further analysis. Images also can be constructed by collecting the ion-induced secondary electron (ISE) signal. These images provide topographical details similar to those observed with a scanning electron microscope.

SIMS images reflect the chemical composition across the surface. For constant primary ion current and assuming a uniform sputtering yield, the SIMS signal from amorphous materials is proportional to the product $N(A)\alpha^{\pm}(A)$, where $N(A)$ is the surface concentration of the selected secondary species A and $\alpha^{\pm}(A)$ is the associated probability for positive or negative secondary particle ionization. The ionization probability is sensitive to surface chemistry: increased surface oxygen content may significantly enhance $\alpha^{+}(A)$.[13,14] Consequently (and perhaps because of matrix effects), we find that the Ga^+ signal from a thick layer of the gallium oxide phase is approximately 15 times greater than that from the clean liquid. In general, the Ga^+ signal from the oxide is lower from thinner films; this relationship remains qualitative without a separate determination of thickness by other techniques. The SIMS technique is reviewed in a recent treatise by Benninghoven, Rüdenauer, and Werner.[15]

B. Sample preparation and analysis

High purity liquid gallium (99.999%, natural isotopic abundances) was spread uniformly over a horizontal stainless-steel substrate as a layer approximately 0.5 mm thick and with area 1 cm^2. The gross oxide skin that naturally forms on liquid Ga was mechanically removed, leaving a reflective, silvery surface. This surface was further cleaned *in vacuo* by ion sputtering, as described below. To avoid possible effects caused by surface topography anisotropies, only the flat center portion of this layer was considered for study. The local curvature was negligible over the analyzed areas, which were about 15 000 times smaller than the total surface.

After inserting the liquid gallium into the SIM, the base pressure of the system was reduced to 2×10^{-9} Torr as measured by a hot cathode ionization gauge (Varian UHV-24 Nude Bayard-Alpert). The partial pressure of O_2 in this base condition was not separately determined. The temperature of the liquid was monitored with a resistive thermometer mounted adjacent to the sample and was, unless noted, $27.7\pm1.0\,^{\circ}C$ throughout the measurements. The Ga at this temperature is slightly supercooled.

At this point, a relatively thick gallium oxide film blankets the liquid. ISE topography images show that the surface has a rough submicrometer-scale structure, occasionally broken by cracks that reveal the pristine liquid below. The oxide is approximately 0.1 μm thick, as estimated by sputtering through the film with the ion probe and noting the sharp drop in Ga^+ signal as the underlying liquid is uncovered (assuming a sputtering yield of 10). The oxide patterns recorded with the O^- SIMS signal are identical to those found with Ga^+, as expected, but are statistically poor (~20 times less signal from the oxide) and therefore difficult to interpret.

Square windows of area A_0 ranging from $(20\ \mu m)^2$ to $(80\ \mu m)^2$ were sputtered through the oxide skin, exposing the clean Ga liquid. The oxygen concentration on the surface in this "clean" condition is not known but is below the detection sensitivity of the instrument, approximately 0.5% for the conditions of this experiment. The oxide surrounding this window forms a rigid frame; the new oxide grows inward from this frame. It is not practical to inspect windows smaller than $(20\ \mu m)^2$ because of instrument-dependent limitations on spatial resolution. Larger windows were not examined because their preparation via sputtering is very time consuming. To check whether the nature of the growth is independent of the shape of the window, the experiment was repeated with circular openings 40 μm in diameter. Occasionally, small oxide peninsulas that jut into the liquid area were intentionally preserved, again to test properties of the growth.

Oxygen (99.9%, dry) was admitted into the SIM at $P=5.0\times10^{-7}$ Torr and, while the primary ion beam was blanked, the oxide growth processes allowed to proceed. For one square window area (40 μm)^2, the experiment was repeated for pressures in the range $1.5\times10^{-8}-1.0\times10^{-6}$ Torr. After a growth interval, the chamber was quickly reevacuated to the 10^{-9} Torr pressure regime and the resulting oxide distribution was imaged by collecting the Ga^+ secondary ion signal. Images were constructed from single 512×512 raster scans. Even with the low primary beam current employed for these analyses, rapid, low-dose [$\sim1.2\times10^{15}$ ions/cm^2 per scan for a (40 μm)^2 window] scans were necessary to minimize damage to the fragile oxide film. Subsequent scans show the oxide phase removed or substantially eroded, indicating that the growths are no more than a few monolayers thick. The windows were recleaned by sputtering before each measurement.

In a separate test of the effect of temperature on oxide growth, the liquid was heated to several temperatures up to 102.0 °C, with a constancy of 1.0 °C at each temperature. Growth (at 5.0×10^{-7} Torr) in square windows with $A_0=(40\ \mu\text{m})^2$ was studied. The opposite experiment, rapidly cooling the liquid to "freeze" the oxide structure, was not performed because of technical difficulties.

C. Interpretation of data

The oxide patterns were measured for total coverage area $C(t)[\mu\text{m}^2]$, perimeter $Per(t)[\mu\text{m}]$, and fractal dimension D. After intensity-level thresholding to discriminate regions covered by oxide from clean liquid, the coverage and perimeter were found and the fractal dimension was computed by a modified box counting procedure, as follows. Each discriminated image was divided into square cells of width L pixels and the number of occupied cells N_L counted. To improve the accuracy of the measurement, N_L was determined for all possible repartitions into $L\times L$ cells and the results were averaged. This counting-averaging procedure was repeated for cells of varying size. If the growth patterns exhibit first-order scaling within some length regime $L_{\min}<L<L_{\max}$, then $N_L=N_0L^{-D}$, where N_0 is an experimental constant related to the coverage of the pattern and D is the box-counting fractal dimension. The error of the measurements, estimated from repeated trials, is 3% for $C(t)$, 5% for $Per(t)$, and ±0.02 for D.

The dimension computed by this algorithm is an approximation of the Hausdorff dimension D_H; $D\geq D_H$. Because of limited spatial resolution, this inequality increases as the oxide pattern becomes dense (such as during late growth). The oxide patterns often display nonuniform dimension, that is, interior branches may have different structure than exterior ones. This calculation produces a measured, *averaged* value for the dimension.

When compared to results from computer simulations of growth and aggregation models, the fractal dimension provides an important clue about the surface oxidation mechanism. The reliability of the calculated dimensions requires additional comment. During the rapid initial stages of growth, when the patterns have the lowest fractal dimension, the oxide spans a small fraction of the total analytical area. Consequently, there is insufficient resolution to examine scaling over more than about 1.5 orders of magnitude, a limited range. At the other extreme, during most of the later growth, the dimension falls between 1.85 to 2.00, where it can be an insensitive gauge of the oxide structure. Nevertheless, we find that the computation consistently differentiates between oxide patterns of, say, equivalent coverage grown on windows of different area, validating the discriminatory power of the procedure.

III. RESULTS AND ANALYSIS

Figure 1 shows the oxide formation over a (60 μm)^2 liquid window as a function of time. In these micrographs, the oxide appears bright, the liquid dark. Initially, lacy disordered branches form along the periphery of the window and along unsputtered oxide peninsulas that may preexist in the growth field [Fig. 1(a)]. These fractal-like structures are anchored to the unremoved oxide, not visible in these views, that surrounds the opening. The independent formation of unattached oxide clusters could not be ascertained. Small ($<0.2\ \mu\text{m}^2$) oxide islands were seen infrequently during the early stages of growth; these islands may have broken and shifted away from the predominant branches. Likewise, interconnections between the oxide filaments during the early stages of growth may be due to slow pivoting and drifting of the monolayer-scale-thick branches.

The oxide develops complex branched patterns as it spreads over the liquid [Figs. 1(b)–1(d)]. During the final growth before the liquid is completely covered, the oxide is crossed by randomly directed, slowly closing gaps. Preexisting peninsulas, marked by greater Ga^+ emission than the new oxide, do not change in size or shape during the growth.

The oxide film is initially thin, with perhaps less than monolayer coverage; all thickness information is qualitative. Enhanced Ga^+ emission from mature oxide indicates that the film gradually thickens. The integrity of these aged films after erosion establishes that they are over a monolayer thick. The Ga^+ SIMS signal from the liquid, and therefore the oxygen concentration, never detectably increased above its $t=0$ s value under any pressure or temperature environment studied. This invariance implies that changes in the liquid surface O concentration, N(O), remain below the detection limit of the instrument.

The oxide growth in the circular windows is similar to that observed in the square ones, indicating that the processes governing the pattern formation are not dependent on macroscopic boundary conditions. The circular windows need not be considered further in this paper.

The oxide coverage as a function of time, $C(t)$, for several different initial window areas A_0, is plotted in Fig. 2(a) ($P=5.0\times10^{-7}$ Torr). For each case, the coverage increases rapidly during the first ~1000 s of growth, then slowly and asymptotically approaches complete coverage. For convenience in this discussion, we arbitrarily divide the growth into "early" and "late" stages (before and after ~1000 s, respectively). It is striking that at any

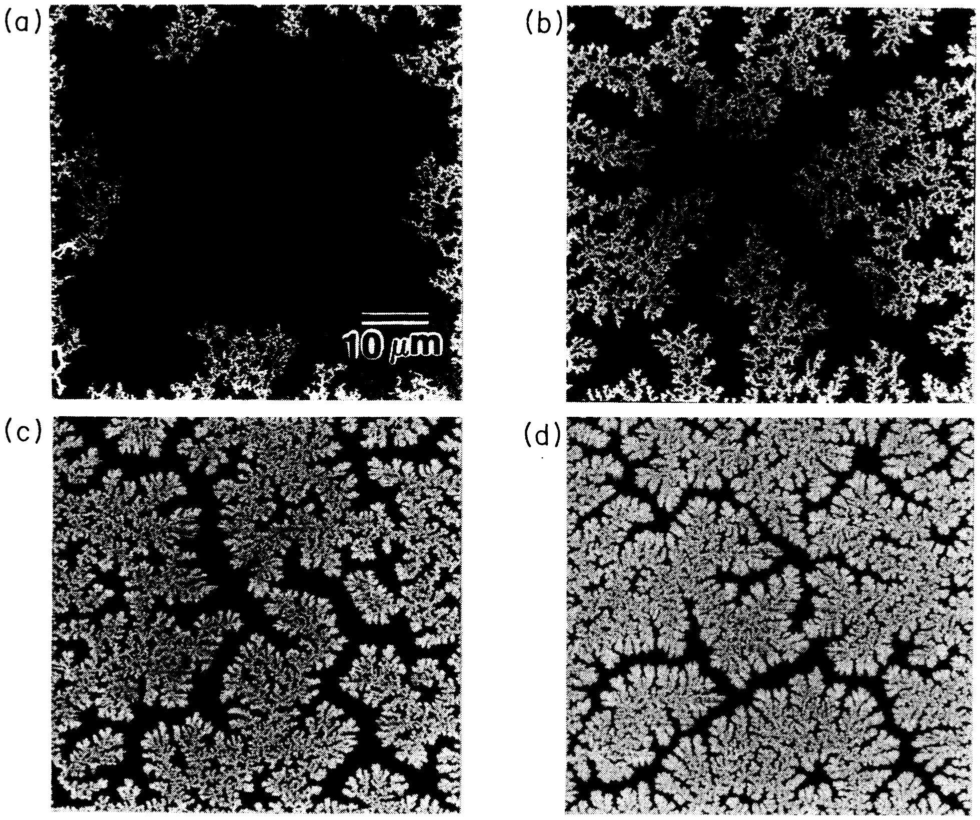

FIG. 1. Gallium oxide growth across cleaned (60 μm)^2 square windows of liquid gallium, imaged with the Ga$^+$ SIMS signal ($P=5.0\times10^{-7}$ Torr, $T=27.7\,^{\circ}\mathrm{C}$). Bright regions correspond to oxide; on the oxide, intensity is related to film thickness. (a) Growth time $t=60$ s, fractional oxide coverage $C(t)/A_0=0.07$, measured dimension $D=1.60$. (b) $t=300$ s, $C(t)/A_0=0.21$, $D=1.68$. (c) $t=1200$ s, $C(t)/A_0=0.51$, $D=1.85$. (d) $t=2400$ s, $C(t)/A_0=0.71$, $D=1.94$. The accuracy of these measurements is discussed in the text.

time, the coverage is greater for larger starting windows, implying that the growth rate is a function of initial boundary area.

The corresponding perimeter data $Per(t)$ is shown in Fig. 2(b). The perimeters increase during the early rapid growth, then (evidently) exponentially decrease as the oxide fills remaining gaps in the liquid. For comparison, an exponential fit through the data $20[A(t)]^{1/2}$ is also plotted, where $A(t)$ is the liquid area and is given trivially by

$$A(t)=A_0-C(t)\ . \tag{1}$$

For this example, the $A(t)$ were derived from the $A_0=(80\ \mu\mathrm{m})^2$ data; reference fits with similar slope are derived for growth in the other examined windows. The factor of 20 merely serves to shift the line to a position where it can be conveniently compared to the perimeter curves. For times greater than about 1000 s, there is general agreement between the slopes of all the curves.

One might expect that the oxide coverage, at least during the initial growth, depends linearly on the perimeter of the growth window. This is not true: after normalizing the coverage data to the initial perimeter of each window, one still finds greater values for oxide growing in larger windows. Similarly, normalizing $C(t)$ to the changing oxide perimeter as a function of time is also unsuccessful. Dividing $C(t)$ by A_0, yielding the dimensionless fractional oxide coverage, gives good agreement between the curves, as shown *mutatis mutandis* in Fig. 3. However, deviations from mutual fit are apparent at early growth times. Similar difficulties are encountered when attempting to interpret the perimeter data. Clearly, a complete understanding of the oxidation must incorporate information about the changing configuration of the oxide film–liquid system.

Toward this goal, the average fractal dimensions of the oxide patterns were examined. Figure 4(a) shows the continuous increase in D as a function of growth time. For clarity, curves for only two initial windows are graphed. Although superficially similar in shape, no trivial linear relationship links the time-dependent dimension and coverage curves.

The increase in measured dimension and time is evident from the micrographs. The oxide begins as a stringy, low-dimension structure [Figs. 1(a) and 1(b)]. As growth progresses, the branches at the growth front (adjacent to the widest liquid gaps) become rounded while the interior branches appear to retain their convoluted, low-dimension form [Fig. 1(c)]. Later, the interior branches also become rounded [Fig. 1(d)]. At this stage, distinct oxide "platelets" become apparent, surrounded by gaps of liquid; the gaps are of roughly uniform width.

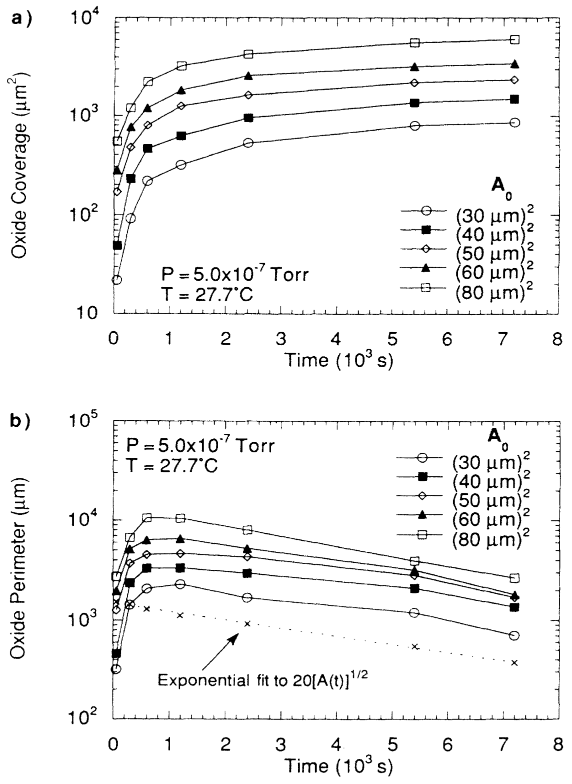

FIG. 2. (a) Increase in oxide coverage $C(t)$ as a function of time, plotted for five different initial window areas A_0. For any given time, the coverage is greater for growth in larger windows. (b) Oxide perimeter $Per(t)$ vs time. For comparison, the $20[A(t)]^{1/2}$ data is included, where $A(t)$ is the liquid area [computed for $A_0=(80\ \mu\mathrm{m})^2$]. To good approximation (for $t \gtrsim 1000$ s), the exponential fit through this data has the same form as the $Per(t)$ vs t curves. The error of each measurement in (a) and (b) is comparable to the size of the plot symbols.

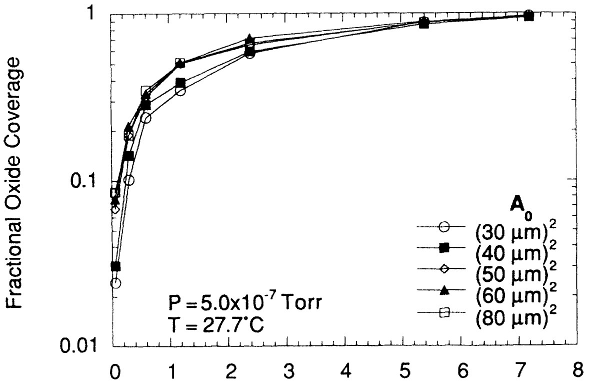

FIG. 3. Fractional oxide coverage $C(t)/A_0$ as a function of time, for five initial window areas A_0. The curves collapse together; compare to Fig. 2(a). For early times, the fractional coverage tends to be greater for growth in larger windows. The error of each measurement is comparable to the size of the plot symbols.

The platelets are separated structures, each lying within a smooth envelope, qualitatively suggesting that a "pressure" is acting against the progression of the growth fronts. Finally, the dimension of the oxide approaches 2.0 as the remaining liquid is slowly engulfed. In general, blunt edges develop first along the outermost branches when they approach the neighborhood of oxide originating from a different portion of the window. This change in fractal structure seems to be localized in a band ringing each platelet. This observation was not checked analytically by a multifractal treatment because of insufficient resolution in the images.

For fixed time, the dimension increases with the area of the starting window [Fig. 4(b)]. This rise is consistent with (but is not a necessary consequence of) the observations noted above; specifically, (i) the greater fractional coverage for larger A_0, combined with (ii) the general increase in D with coverage that is apparent in the micrographs and Fig. 4(a).

It is instructive to recast the liquid area and perimeter data as $A(t)/Per(t)$, plotted as a function of time (Fig. 5). This graph dramatically shows the rapid increase in perimeter (compared to liquid area) during the initial

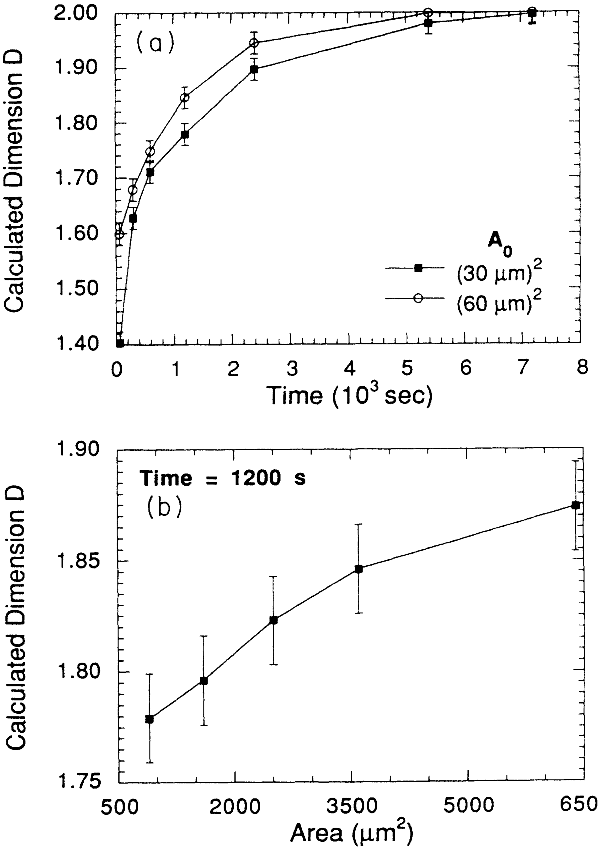

FIG. 4. Measured fractal dimension of the oxide patterns as a function of (a) growth time and (b) initial window area A_0 ($P=5.0\times10^{-7}$ Torr, $T=27.7\,^{\circ}\mathrm{C}$). As the oxide engulfs the liquid at large times, the dimension approaches 2.00, as expected. For given time, the dimension is slightly larger for growth in larger windows.

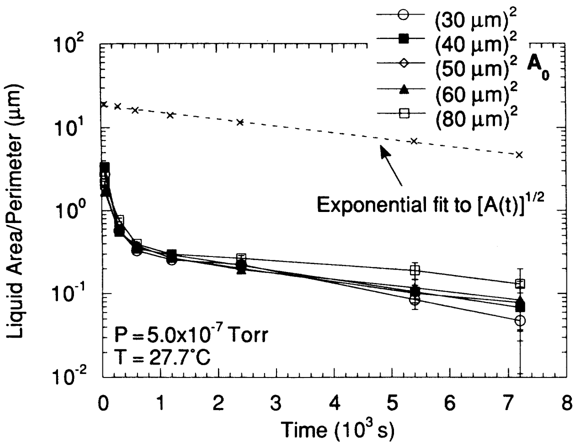

FIG. 5. Ratio of liquid area to perimeter $A(t)/Per(t)$, as a function of time. The $[A(t)]^{1/2}$ data is drawn for reference [computer for $A_0=(80\ \mu m)^2$]. The slopes of all curves are comparable for times $\gtrsim 1000$ s.

low-dimension growth. For uniform $D=2.0$ growth, we expect the perimeter to be proportional to the square root of the liquid area,

$$Per(t) \propto [A(t)]^{1/2}, \tag{2}$$

and therefore $A(t)/Per(t) \propto [A(t)]^{1/2}$. Accordingly, the $[A(t)]^{1/2}$ data are drawn for comparison [computed for $A_0=(80\ \mu m)^2$]; an exponential fit through this data is included. The expected constant proportionality is observed for times greater than about 1000 s. The exponential time dependence of the curves is explicated in Sec. IV B. The constant ratio at late times between each $Per(t)$ and the reference curve in Fig. 3(b) is a concomitant consequence of Eq. (2).

The relationship between pressure and fractional oxide coverage (for fixed time and A_0) is shown in Fig. 6. A linear fit satisfactorily describes the data. Also plotted is the exponential fit

$$C(P)/A_0 = 1 - \exp(-kP), \tag{3}$$

where $k \approx 1.6 \times 10^6$ Torr^{-1}. The $P = 5 \times 10^{-7}$ Torr measurement deviates from this curve by approximately 50%.

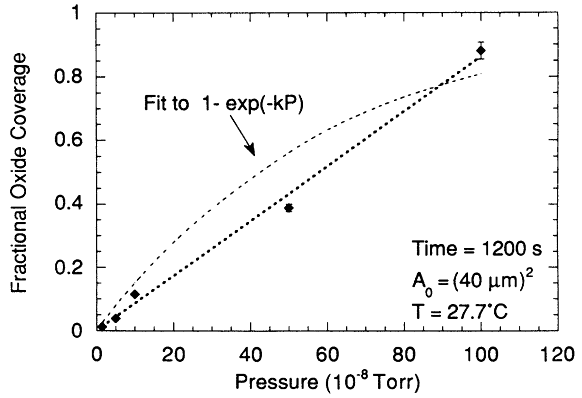

FIG. 6. Fractional oxide coverage $C(P)/A_0$ vs ambient O_2 pressure. A linear (least squares) fit to the data is shown, along with the fit to the equation $1-\exp(-kP)$. The constant k, as shown, is 1.6×10^6 Torr^{-1}. The accuracy of this value, as well as the justification for the exponential fit, are discussed in the text.

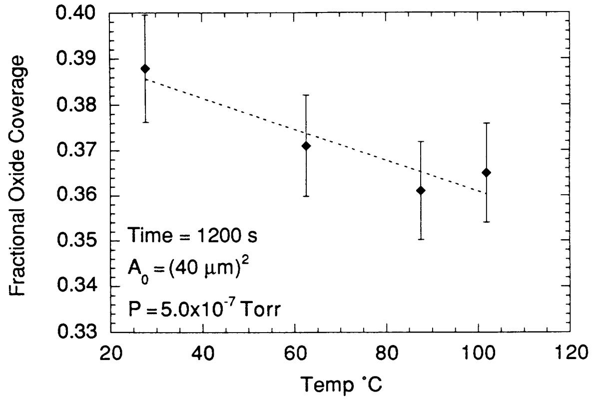

FIG. 7. Fractional oxide coverage $C(T)/A_0$ as a function of liquid temperature, for fixed time. There is a downward trend in the data for increasing temperatures. The dashed straight line is for reference only. The observed reduction in fractional coverage from minimum to maximum temperature is consistent with the prediction presented in this paper [Sec. IV B, Eq. (7)].

The fractional oxide coverage $C(T)/A_0$ tends downward slightly with liquid temperature [Fig. 7, $t=1200$ s, $A_0=(40\ \mu m)^2$]. A straight reference line is included to guide the eye. The uncertainty in the measurements prohibits a precise determination of this relationship.

IV. DISCUSSION

To understand the oxide growth, three fundamental aspects of the observed phenomena must be addressed: (1) What aggregation mechanism is responsible for the disordered, isotropic oxide branching during early growth? (2) How is the oxide coverage related to growth time, liquid temperature, ambient oxygen pressure, and original window area? (3) Why is the late growth distinct from early growth? In particular, why does the oxide structure become denser, and why do uniform gaps form between the oxide platelets?

A. Aggregation mechanism

The fractal-like structure of gallium oxide as it forms on liquid gallium, at least during the early stages of growth, is not observed during oxidation on solid surfaces. Indeed, when this experiment was repeated on solid Ga, the oxide developed homogeneously across the cleaned window, superimposed over enhanced oxidation at localized sites on the surface (possibly steps, dislocations, impurities, or grain boundaries that act as nucleation centers). During oxidation on the liquid, the unvarying size and shape of preexisting peninsular structures indicate that the oxide is being created within the analytical area, and is not creeping into the cleaned window from the oxidized surroundings. The randomly dispersed, nondendritic oxide branches suggest that the patterns are formed during nonequilibrium growth. We are motivated by this accumulated evidence to propose that the early growth is the result of a diffusion-limited aggregation process (DLA).[16] In this picture, diffusing particles random walk across the liquid until they contact the oxide perimeter, sticking with some probability. This proposal is buttressed by the visual similarity between the early oxide patterns (with dimension 1.6–1.8) and countless computer simulations of DLA growth in two dimensions (which give $D=1.7$).[17]

The characteristic "X" gap pattern that develops during oxidation is a natural result of the reduced probability for diffuser migration into the corners of the window [see Figs. 1(c) and 1(d)], when growth is controlled by a scalar diffusion field that obeys the Laplace equation.[16] During later growth, the corners are shadowed from the diffusing particles by structures growing along the window edges.

The diffusing particle and diffusion field must be determined. Heat dissipation from the forming gallium oxide front can be ignored. The micrometer-size growth windows, the apparent slow oxide formation, and the large heat capacity of the underlying liquid, militate against the significance of heat diffusion. Chemical diffusion fields, such as a gradient of impurities across the liquid, were searched for but not detected. Hydrogen and hydrocarbons, which are residual ultrahigh vacuum contaminations, were detected on both the cleaned liquid and oxide but at levels too low for satisfactory evaluation. Any concentration gradients across the liquid, or changes with time, were below the sensitivity of the instrument. Common environmental contaminations such as sodium were not associated with the oxide patterns.

It is probable that oxygen itself is the diffusing particle, migrating over the liquid until impacting on growing oxide. At room temperature, molecular oxygen dissociates and chemisorbs on solid gallium[18] and aluminum,[19] and presumably on liquid Ga also. The population of chemisorbed oxygen on the liquid Ga film is not known. Su *et al.*[5] report that a weak oxide feature is visible in the photoemission signal from a film of Ga after an exposure of 100 L O_2, which corresponds to 200 s at 5×10^{-7} Torr O_2. This broad-area measurement does not take into account the localization of oxide that is observed in the present experiment. To first approximation, this photoemission result implies that the combined gas-to-liquid sticking-desorption probability S is less than 10^{-2}, for low oxygen coverage on the liquid. We self-consistently derive below, from the oxide growth data, $S\sim10^{-3}$. The total oxygen content on the liquid is unknown, but as noted in Sec. III, does not detectably increase above its $t=0$ value. Based on these observations, it is reasonable to regard the chemisorbed O as a dilute "surface gas." The oxide growth is limited by the supply and diffusion of O to the growing structure.

The mean-free path of oxygen over the surface of the liquid is comparable to that of the underlying liquid particles, i.e., less than the mean atomic spacing in the liquid.[20] The surface diffusion coefficient for oxygen on liquid gallium is not known. Starting with the self-diffusion coefficient for bulk liquid Ga ($D_B=1.7\times10^3$ $\mu\mathrm{m}^2\,\mathrm{s}^{-1}$),[21] one can estimate a diffusion coefficient of 3×10^3 $\mu\mathrm{m}^2\,\mathrm{s}^{-1}$ for O in Ga. Because there is much less space for the diffusing particle to explore on the surface, the surface diffusion coefficient will be larger; an exact value cannot be deduced without a better understanding of liquid metal surfaces. References 22 and 23 present some current discussions about liquid metal surfaces. In solids, the coefficient for self-diffusion at the surface can be 10^5 times larger than in the bulk.[24] To get a sense of the speed of this diffusion, the average lateral O migration distance in one second is greater than the approximate value in the bulk, conservatively $1.7(D_B t)^{-1/2}\approx90$ μm. This distance is larger than the dimension of all windows examined.

Furthermore, an increase in the liquid temperature would lengthen the diffusion distance per unit time. Over the temperature range of this experiment, one calculates that D_B increases by a small factor, ~1.4. Diffusion over the surface presumably also increases slightly. In sum, the chemisorbed O wanders rapidly within the boundaries of the windows examined in this experiment, visiting the oxide or preexisting structures in negligible time.

The diffusing oxygen adheres to the oxide perimeter with probability λ, which is related to the oxidation activation energy E_A. The activation energy may be a function of liquid temperature; this functionality could not be disentangled from the other operant parameters over the limited temperature range of this experiment.

The growth is the result of a multiparticle aggregation process, where a finite number of particles diffuse simultaneously over the liquid. Fractal correlations in structures formed through this process extend to a characteristic correlation length ξ. This length is related to the population of diffusing particles (ρ) by $\xi\sim\rho^{-\gamma}$ ($\rho=1$ denotes the maximum possible concentration of diffusers on the liquid). The exponent γ is not well characterized but is approximately equal to 3.[25] At length scales less than ξ, the structure is DLA-like ($D\approx1.7$); for larger lengths, D approaches 2. In this experiment, ρ, which is related to the low surface oxygen concentration $N(\mathrm{O})$, is unknown. The data suggest that for this experiment $\rho\ll1$. During early growth, fractal scaling exists from the smallest resolvable size up to dimensions on the order of the window width. The observed increase in measured dimension with growth occurs at small lengths; this increase is discussed in Sec. IV C.

There is no evidence that the mobile oxygen particles interact to form large diffusing clusters. The fractal dimension that characterizes cluster-cluster aggregation (<1.5, determined via simulations[26,27]) is only found for the shortest growth time examined in this experiment ($t=60$ s at $P=5.0\times10^{-7}$ Torr). It is feasible that unresolvable cluster form and migrate across the liquid. Meakin finds that aggregation with Levy-Flight trajectories can produce dimensions between 1.7 and 2.0.[28] However, the dense patterns so generated do not resemble the oxide, even during late growth. For the most straightforward description of the oxidation process, it is unnecessary to introduce this elaboration.

B. Oxidation kinetics

The oxide coverage kinetics can now be understood as the result of a three-step process: gas-to-liquid adsorption, followed by O migration across the liquid, and finally O incorporation onto the growing oxide perimeter. We now address the specific physical mechanisms that govern these processes.

The rate at which O_2 molecules are adsorbed on the liquid surface per area at 27.7 °C is given by[29]

$$R = 3.6\times 10^{12}\ PS(\theta)\ \ [\mu\text{m}^{-2}\text{s}^{-1}]\ , \qquad (4)$$

where P is the gas pressure in Torr and $S(\theta)$ is the combined gas-to-liquid sticking–desorption probability. This probability is expressed as a function of the fractional oxygen adsorption on the liquid, θ (that is, the fraction of possible oxygen adsorption sites on the liquid that are occupied). This fraction is proportional to N(O). The absence of a detectable change in Ga^+ signal from the liquid during this experiment indicates that θ is $\ll 1$, and hence we take $S(\theta)=S$, a constant (for fixed P and T). The adsorption rate depends on temperature as $R \propto T^{-1/2}$ (Ref. 29).

As a simplification that is consistent with the data, we assume that the average concentration of oxygen on the liquid rises rapidly to a constant equilibrium value, N(O, steady state); in other words, the steady-state fractional oxygen adsorption θ is constant. (This does not imply equilibrium growth.) Of course, any concentration gradient arising from the diffusion-aggregation process still exists. Any increase in chemisorbed O is balanced by incorporation into the oxide. This perfect transfer of O from the gas to the oxide is a consequence of the growth being limited by the demonstrably scarce supply of diffusing O. Because of the rapid O migration, this transfer occurs in negligible time, compared to the measurable growth intervals. The rise time to this steady state is on the order of the time required for the migrating O to traverse the growth window.

In this steady-state condition, the *effective* oxide formation probability is 1: all oxygen newly deposited onto the liquid is incorporated into the oxide. This effective probability can be expressed as $(\lambda v)=1$, where we factor out λ to emphasize that it is still a variable. The second factor v (in this case equal to λ^{-1}), will be less than λ^{-1} if the supply of O per unit time exceeds the incorporation rate of the oxide.

In this concentration equilibrium regime, the change in oxide film coverage $dC(t)$ is

$$dC(t) = G\lambda vR\,A(t)dt\ , \qquad (5)$$

where G is a geometric conversion factor giving the increase in oxide area for each incorporated oxygen atom. As a rough approximation, we adopt $G \approx 6$ Å$^2 = 6\times 10^{-8}$ μm^2, the value for a monolayer of β-Ga_2O_3.[30] This figure is typical for crystalline or amorphous solids. The thickness of the oxide film is not known, but as noted in Sec. II B varies from less than a monolayer at early times to a few monolayers later.

Equation (1) implies $dA(t) = -dC(t)$. With Eq. (5), this leads to

$$A(t) = A_0 \exp(-G\lambda vRt)\ . \qquad (6)$$

The remaining liquid area, expressed as a fraction of the original window size, $A(t)/A_0$, is plotted as a function of time in Fig. 8 (for $P=5.0\times 10^{-7}$ Torr). The data collapse onto a common curve. Here, deviations from mutual fit at early times in the $C(t)/A_0$ vs time graph (Fig. 3) are inconspicuous because of the logarithmic representation. The average slope (excluding the early growth data) is $G\lambda vR = (4.0\pm 0.3)\times 10^{-4}\ \text{s}^{-1}$, from which we derive 6500 $\mu\text{m}^{-2}\text{s}^{-1}$ for the combined parameters λvR. This is the number of oxygen atoms incorporated into the oxide each second per 1 μm^2 liquid area, at this pressure. We do not provide an error for this value because of the inexact estimate for G. The exponential behavior of the $Per(t)$ and $A(t)/Per(t)$ vs time curves [Figs. 2(b) and 5], at times greater than about 1000 s, can now be understood in terms of Eq. (6) and the proportionality between $Per(t)$ and $[A(t)]^{1/2}$ for uniform two-dimensional growth [Eq. (2)].

Equation (6) must be corrected if G is not constant; the consistency of the late-growth data (taken with the uncertainty in the measurements) does not mandate this correction. Equation (6) will still hold if the effective oxidation probability (λv) is a constant less than 1. In this situation, the growth is no longer limited by the supply of O, and N(O) will increase. This (undetected) increase in N(O) would affect the oxide pattern formation, notably by reducing the correlation length over which DLA-like scaling holds.[25]

Assuming $(\lambda v)=1$, then the sticking–desorption probability, calculated from the slope of Fig. 8 and Eq. (4), is $S(\theta) = 1.8\times 10^{-3}$ (at 5.0×10^{-7} Torr, 27.7 °C). This number is in accord with the estimate derived from the photoemission data.[5] We again express S as a function of

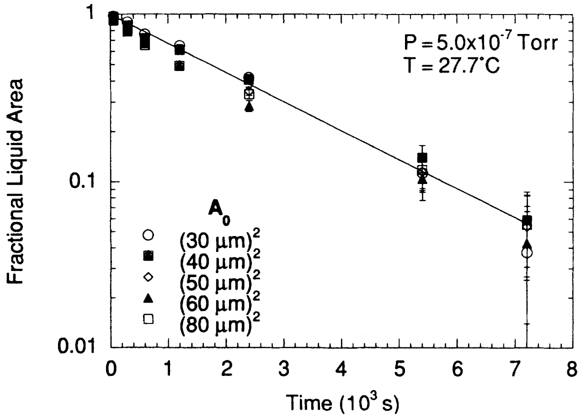

FIG. 8. Fractional remaining liquid area $A(t)/A_0$, graphed as a function of time for five different initial window areas. With good agreement, the data fall on one decreasing exponential curve, $A(t)/A_0 = \exp(-\text{slope}\ t)$, where slope$=(4.0 \pm 0.3)\times 10^{-4}\ \text{s}^{-1}$. This value was determined by averaging the exponential fits (least squares) through the data for each A_0.

θ, to allow the possibility that N(O, steady state), and therefore S, may vary with temperature or gas pressure.

From Eqs. (1), (4), and (6) we can retrieve Eq. (3). For fixed A_0, temperature, and time,

$$C(P)/A_0 = 1 - \exp(-kP) \ . \tag{3}$$

We now see that k is 3.6×10^{12} $GS\lambda t$ [Torr^{-1}], which from Fig. 6 was found to be approximately 1.6×10^{6} Torr^{-1} ($t=1200$ s). Alternatively, k can be derived from the slope of Fig. 8: equating the exponential terms in Eqs. (3) and (6), and setting $t=1200$ s and $P=5\times10^{-7}$ Torr (the appropriate parameters for the data displayed in Figs. 6 and 8), we obtain $k=9.4\times10^{5}$ Torr^{-1}, in close agreement with the value determined from Fig. 6.

It is unclear why the fractional coverage vs pressure data (Fig. 6) only weakly fit the derived exponential form; perhaps a better fit would be found if more statistics were accumulated. Speculatively, the steady-state O concentration (and therefore θ) on the liquid may vary with P; this variation could be large enough to influence $S(\theta)$. Nevertheless, it is encouraging that the coefficient k derived from two distinct procedures is constant within a small factor.

The ratio of oxide coverages for the maximum to minimum temperatures examined is, from Eqs. (1) and (6), and with the temperature dependence of R and the slope of Fig. 8:

$$\frac{C(T_{\max})}{C(T_{\min})} = \frac{1-\exp(-8.1T_{\max}^{-1/2})}{1-\exp(-8.1T_{\min}^{-1/2})} = 0.92 \ , \tag{7}$$

for $t=1200$ s, $P=5\times10^{-7}$ Torr, and assuming constant $S(\theta)$. This predicted 8% decrease with temperature is consistent with the measurements.

C. Pattern development during late growth

The simple diffuse–aggregate model that describes the oxide patterning during early growth must be augmented to account for the dense, rounded structures observed later. The gradual, continuous increase in fractal dimension, ascertained by both visual and analytical inspection of the data, is unusual (in many other systems, there exists a sharp crossover between DLA-like and D-increasing growth). If this transition exists in the oxidation system, it may occur during the rapid initial growth (<300 s), before the pattern starts to become "compact." Repeated measurements separated by small time steps are required to detect this possible transition.

Given the bounded geometry of this experiment, it is not surprising that the measured oxide dimension approaches 2.0 with growth. The region available for growth shrinks with time: there must be a transition from the initial low-dimension branches to the ultimate two-dimensional oxide crust. Any remaining structure within the final film, for example, a fine network of cracks, is on a scale too small to be detected by the technique. It is obvious that simple DLA growth cannot be maintained in the confined area of the growth windows: the area of a DLA structure in an open two-dimensional field goes as $C(t)\propto t^{1.0}$ (single-particle aggregation), with an unlimited maximum size.[31] The maximum lateral extent of each oxide platelet in this experiment is constrained to approximately half the width of the window.

Holes and channels within the later-growth structure can be filled by oxygen adsorption onto neighboring liquid, rather than by O diffusion from distant regions. Competition between adjacent fingers becomes important as they inevitably converge together on the diminishing liquid area. Importantly, it is likely that the disposition of the aggregation changes as the growths approach closer than a characteristic diffusion length. Because of these complexities, a complete theoretical formulation of growth in the geometry of this experiment is wanting.

Simulations of the aggregation of single-particle random walkers on a bounded 256×256 square lattice ($\lambda=1$) display some features similar to those observed in this experiment.[6] Not surprisingly, the simulations show an increase of the box-counting dimension with growth. However, the simulations do not predict the rounding of the platelet edges, nor the formation of uniform gaps between the platelets. Variations of the related multiparticle, multiple-growth-site simulations reported by Witten and Meakin[32] might yield patterns similar to those observed in this experiment. Couder[33] performed DLA simulations within a circle of finite radius. Although the pattern evolution he computed is unlike "classical" DLA growth (reduced side branching, etc.), he does not note the structures observed in the present experiment. It is likely that some mechanism beyond this simple diffuse-aggregate process, unpronounced during the early, low-dimension growth, becomes significant as the liquid area is diminished.

Close examination of the platelet–liquid gap region provides insight into this additional mechanism. Two features are notable in photographically enlarged views of later-growth platelet edges (Fig. 9). First, morphologically distinct elongated oxide fingers occur in a narrow band along the periphery of each oxide platelet [an example is indicated in Fig. 9(a)]. There fingers run perpendicular to the broad liquid gaps. The oxide in the interior of the platelets has a different structure, with narrow interconnected channels and pores. Second, enhanced Ga^{+} emission from this fingered periphery indicates that the film is thicker or denser there than in its interior (or that there is an increased concentration of oxygen within the oxide along the periphery). This enhanced emission is clearly seen as a band edging the platelets in Fig. 9(a). Short, narrow, tributary gaps, often attached at right angles to the wider gaps, are seen during the terminal growth [Fig. 9(b)].

We conjecture that an impurity (or several impurities), insoluble in the oxide, accumulates on the liquid as it is excluded from the growing film. The average concentration of the impurity increases as it is confined to a decreasing liquid area. It is possible that this concentration may be nonuniform over the liquid. Nevertheless, the growth fronts of all the platelets have similar morphology because (to first order) they were exposed during growth to equivalent impurity environments. The net oxide growth rate does not seem to be affected by the changing impurity concentration, as evidenced by the continuous exponential decrease in liquid area; however, it cannot be

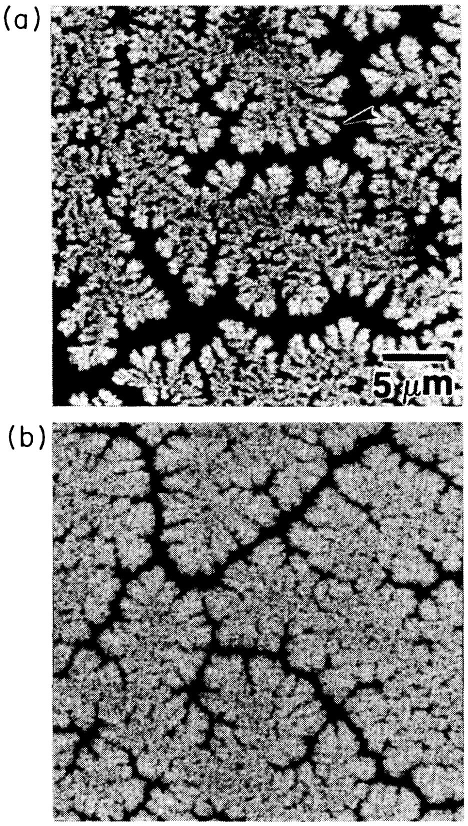

FIG. 9. Oxide growth fronts during late growth ($P = 5.0 \times 10^{-7}$ Torr, $T = 27.7\,^\circ\mathrm{C}$). Each image is a detail of growth in an $A_0 = (80\ \mu\mathrm{m})^2$ window. (a) Growth time $t = 2400$ s, fractional oxide coverage $C(t)/A_0 = 0.67$, measured dimension $D = 1.94$. The thicker (brighter) oxide platelet rims are evident. A typical oxide finger within this thick region is indicated. (b) $t = 5400$ s, $C(t)/A_0 = 0.88$, $D = 1.99$. Uniform-width gaps in the oxide traverse the growth window.

ruled out that small variations in the oxidation rate are hidden by the scatter in the data. The nature of the impurity could not be determined. The average impurity concentration need not exceed that for the chemisorbed oxygen, and therefore may be below the detection limit of the instrument.

We propose two processes, perhaps both occurring, that are driven by this proposed impurity and that may be responsible for the observed non-DLA characteristics. The rounded form of the growth fronts indicate that interfacial surface tension of some kind, and possibly oxide reordering, may be active during late growth. These effects, taken to be zero in the DLA picture, can stabilize the oxide–nonoxide interface. The finger-like oxide bulges resemble features observed in dense branching morphology (DBM) growth, described by Ben-Jacob *et al.*[34,35] which is a consequence of these additional factors.

Further experiments are necessary to determine how the conjectured impurity affects the interface dynamics. As one possibility, it is not unreasonable that there exists an impurity concentration gradient over the liquid that is related to the local curvatures of the growth fronts. The impurity may compete with the diffusing oxygen for available growth sites, reducing λ. This competition will vary along the interface according to the local concentration and gradient of the impurity. In this scenario, well-described instability methodologies accrue.[36–38] Under the proper conditions (growth rate, impurity concentration, and gradient), this process will slow growth at the oxide tips, producing a smooth interface. The dense branching is not apparent during the early oxide growth [Figs. 1(a) and 1(b)], indicating that there is some concentration threshold below which the impurity has negligible influence.

Dense branching that occurs during the annealing of Al-Ge films is caused by a change of phase structure and crystallinity within the structure.[39] In the present experiment, the apparent increase in thickness of the rounded oxide fingers may be a sign that they have a different internal structure than the nonfingered film. If they are ordered crystallites, rather than amorphous, then anisotropic dendritic growth may occur, leading to a dense-branched appearance. The crystal structure of the oxide cannot be characterized easily. It is not clear how the conjectured impurity would initiate this transition in the oxide.

As a concurrent smoothing process, the increase in average impurity concentration may lead to a global reduction in the oxide sticking probability λ. This reduction allows the diffusing particles to fill the growing structure more efficiently, broadening the oxide branches.[40] Examining sputter-deposited $\mathrm{NbGe_2}$ films, Elam *et al.*[41] observed cluster broadening, and speculated that it is the result of a gradual decrease in λ as the film thickens vertically during growth. They calculate (from the density-density correlation function) an effective fractal dimension greater than 1.8. Slightly different simulations by Meakin of single-particle aggregation indicate that the Hausdorff dimension is insensitive to λ (i.e., $D \approx 1.7$ for aggregation in a plane), if λ is a constant between 0.1 and 1.[42] Apart from this difference in dimension, the broadened patterns presented by both groups are reminiscent of the oxide finger structures observed in this experiment. Multiparticle aggregation with $\lambda < 1$ also gives denser, rounded growth.[43] The oxide sticking probability may decrease because of an associated structural change in the thicker platelet rim. The persistent exponential decrease in liquid area suggests that the effective oxide formation probability (λv) is unity, i.e., the growth remains limited by the scarce supply of diffusing O.

There is no evidence that, in the absence of diffusing oxygen, oxide dissolution or reconstruction processes cause the oxide perimeter to become rounded. When the oxide was grown at minimum pressure ($P \sim 2 \times 10^{-9}$ Torr) for long periods ($> 4 \times 10^4$ s), filamentary patterns developed similar to those seen in Fig. 1(a). This apparently amorphous structure, formed and existing over an extended time, manifests little tendency for rounding via dissolution or ripening. Also, patterns formed at high pressure ($> 10^{-8}$ Torr) and preserved for several hours at minimum pressure before observation are indistinguishable (in terms of oxide coverage, perimeter, and dimension) from patterns measured immediately after growth.

This constancy indicates that the oxide is highly stable at low ambient pressures, even when high concentrations of the conjectured impurity are present. Whether this stability is deleteriously affected by a large oxygen concentration on the liquid surface is unknown.

There is evidence that the oxide in the interior of the platelets reorders during late growth, perhaps to a polycrystalline form. The oxide film is uniformly thick, except at the narrow periphery. If there were no oxide reordering, the oxide would grow progressively thicker toward the periphery, within the band swept by the growth front. This gradient in thickness is not observed. Direct adsorption from the gas to the top surface of the oxide, which has not been considered in this report, may also contribute to this process. As the film thickens, G (the conversion factor giving the increase in oxide area for each incorporated oxygen atom) gets smaller. In part, the small deviations from mutual fit in the fractional coverage data (Fig. 3) for early times may be due to different onset times for this change in G. We must reiterate that the "thick" oxide is only a few monolayers deep.

V. SUMMARY AND CONCLUSION

We propose that an isotropic, nonequilibrium diffusion aggregation process is responsible for gallium oxide growth across liquid Ga, for ambient O_2 gas pressures $\leq 1 \times 10^{-6}$ Torr, and for liquid temperatures between 27.7 and 102.0 °C. The observed fractal-like pattern formation is modified during late growth, perhaps by the presence of an impurity that is insoluble in the oxide, introducing interfacial smoothening. The data are consistent with the hypothesis that oxygen is the diffusing particle. After being chemisorbed at a dilute concentration onto the liquid, the oxygen random walks until it impinges upon existing oxide, where it is incorporated irreversibly (with varying probability) into the structure, causing the lateral extension of the oxide. Changes in the concentration of O on the liquid were too small to measure with the present SIMS instrument. Analysis of the oxide coverage as a function of time suggests that the O concentration on the liquid surface reaches a steady-state value, when all O added to the surface by adsorption–desorption is transferred to the growing oxide edge. It could not be ascertained whether there is interaction between the diffusing particles.

The finite area of the growth windows imposes restrictions on the oxide growth kinetics. During late growth, the fractional liquid area $A(t)/A_0$ exponentially decreases with time, in accordance with the model proposed here. Small discrepancies during the early, low-fractal-dimension growth may be due to changes in the thickness of the oxide film. The observed change in fractional oxide coverage $C(T)/A_0$ with temperature is also consistent with the model. Further measurements are required to verify the expected exponential relationship between fractional oxide coverage and pressure.

Some process that is associated with the reduced liquid area instigates changes in the oxide patterns: the oxide perimeters become rounded, apparently repel each other, and are separated by uniform gaps. An impurity, confined to the liquid, may cause these effects, perhaps by promoting interfacial tension or oxide reordering. The oxide-sticking probability may also be reduced. It is probable that the diffuse-aggregate process is modified as the growth edges approach one another closer than some critical distance related to the surface O and impurity concentrations.

Additional research is necessary to resolve remaining questions about the oxidation process. Alterations in the oxidation process (and pattern formation) can be studied following the controlled addition of impurities to the liquid or surrounding gas. As a related concern, the steady-state oxygen content on the liquid, if one exists, should also be determined. By combining the results of imaging SIMS and other surface analysis techniques, it may be possible to determine accurately the oxygen mobility over the liquid surface, and the oxidation activation energy E_A.

This experiment is an excellent start toward understanding the kinetics and lateral development of gallium oxide over liquid gallium. The fractal-like pattern formation has not, to our knowledge, been observed by any technique other than imaging SIMS. In general, the spatial distribution of oxidation on liquids is an unexplored topic. The methods developed for this experiment can be extended to the study of a wide family of liquid metal systems. As an example, it is of interest to investigate the competitive formation of oxides on binary alloys. Experiments of this kind are underway.

ACKNOWLEDGMENTS

This research would not have been possible without the patience and guidance of Professor Riccardo Levi-Setti, and without helpful discussions with my colleagues at The University of Chicago. This report is based on research supported by the NSF Materials Research Laboratory at the University of Chicago.

---

[1] A. Rahmel, G. C. Wood, P. Kofstad, and D. L. Douglass (editors), Oxid. Met. **23**, 251 (1985).

[2] P. Kofstad, A. Rahmel, R. A. Rapp, and D. L. Douglass (editors), Oxid. Met. **32**, 125 (1989).

[3] For example, see A. J. Bevolo, J. D. Verhoeven, and M. Noack, Surf. Sci. **134**, 499 (1983).

[4] A. Roth, *Vacuum Technology* (North-Holland, Amsterdam, 1982), p. 158.

[5] C. Y. Su, P. R. Skeath, I. Lindau, and W. E. Spicer, Surf. Sci. **118**, 248 (1982).

[6] Y. L. Wang, A. Raval, and R. Levi-Setti, Scanning Microsc. **3**, 731 (1989).

[7] J. M. Chabala and R. Levi-Setti, in *Secondary Ion Mass Spectrometry VII*, edited by A. Benninghoven (Wiley, New York, 1992), p. 549.

[8] R. Levi-Setti, Y. L. Wang, and G. Crow, J. Phys. (Paris) **45**, C9-197 (1984).

[9] J. M. Chabala, R. Levi-Setti, and Y. L. Wang, J. Vac. Sci.

Technol. B **6**, 910 (1988).

[10] J. M. Chabala, R. Levi-Setti, and Y. L. Wang, Appl. Surf. Sci. **32**, 10 (1988).

[11] P. Sigmund, Nucl. Instrum. Methods B **27**, 1 (1987).

[12] P. Sigmund *et al.*, Nucl. Instrum. Methods B **36**, 110 (1989).

[13] G. Slodzian and J.-F. Hennequin, C. R. Acad. Sci. Paris B **263**, 1246 (1966).

[14] A. Benninghoven and A. Mueller, Phys. Lett. **40A**, 169 (1972).

[15] A. Benninghoven, F. G. Rüdenauer, and H. W. Werner, *Secondary Ion Mass Spectrometry* (Wiley, New York, 1987).

[16] T. A. Witten, Jr. and L. M. Sander, Phys. Rev. Lett. **47**, 1400 (1981).

[17] P. Meakin, Phys. Rev. A **27**, 604 (1983).

[18] D. Schmeisser and K. Jacobi, Surf. Sci. **108**, 421 (1981).

[19] P. Hoffmann, K. Horn, A. M. Bradshaw, and K. Jacobi, Surf. Sci. **82**, L610 (1979).

[20] J. S. Kirkaldy and D. J. Young, *Diffusion in the Condensed State* (The Institute of Metals, London, 1987), p. 93.

[21] P. Protopapas, Hans C. Andersen, and N. A. D. Parlee, J. Chem. Phys. **59**, 15 (1973).

[22] J. G. Harris, J. Gryko, and S. A. Rice, J. Chem. Phys. **79**, 5658 (1987).

[23] W. Schommers, in *Structure and Dynamics of Surfaces II,* edited by W. Schommers and P. von Blanckenhagen (Springer-Verlag, Berlin, 1987), p. 223.

[24] G. E. Rhead, Int. Mater. Rev. **34**, 261 (1989).

[25] P. Meakin, Physica A **153**, 1 (1988).

[26] M. Kolb, R. Botet, and R. Jullien, Phys. Rev. Lett. **51**, 1123 (1983).

[27] P. Meakin, Phys. Lett. **51**, 1119 (1983).

[28] P. Meakin, Phys. Rev. B **29**, 3722 (1984).

[29] S. Dushman and J. M. Lafferty, *Scientific Foundations of Vacuum Technique* (Wiley, New York, 1962), p. 14.

[30] R. W. G. Wyckoff, *Crystal Structures,* 2nd ed. (Wiley, New York, 1964), Vol. 2, p. 13.

[31] R. F. Voss, Phys. Rev. B **30**, 334 (1984).

[32] T. A. Witten and Paul Meakin, Phys. Rev. B **28**, 5632 (1983).

[33] Y. Couder, in *Random Fluctuations and Pattern Growth,* edited by H. E. Stanley and N. Ostrowsky (Kluwer Academic, Dordrecht, 1988), p. 75.

[34] E. Ben-Jacob, G. Deutscher, P. Garik, Nigel D. Goldenfeld, and Y. Lareah, Phys. Rev. Lett. **57**, 1903 (1986).

[35] E. Ben-Jacob and P. Garik, Nature (London) **343**, 523 (1990).

[36] J. S. Langer, Rev. Mod. Phys. **52**, 1 (1980).

[37] D. A. Kessler, J. Koplik, and H. Levine, Adv. Phys. **37**, 255 (1988).

[38] D. A. Kessler and H. Levine, Phys. Rev. Lett. **67**, 3121 (1991).

[39] G. Deutscher and Y. Lareah, Phys. Rev. Lett. **60**, 1510 (1988); S. Alexander, R. Bruinsma, R. Hilfer, G. Deutscher, and Y. Lareah, *ibid.* **60**, 1514 (1988).

[40] T. A. Witten and L. M. Sander, Phys. Rev. B **27**, 5686 (1983).

[41] W. T. Elam, S. A. Wolf, J. Sprague, D. U. Van Vechten, G. L. Barz, Jr. and P. Meakin, Phys. Rev. Lett. **54**, 701 (1985).

[42] P. Meakin, Phys. Rev. A **27**, 1495 (1983).

[43] R. F. Voss, J. Stat. Phys. **36**, 861 (1984).

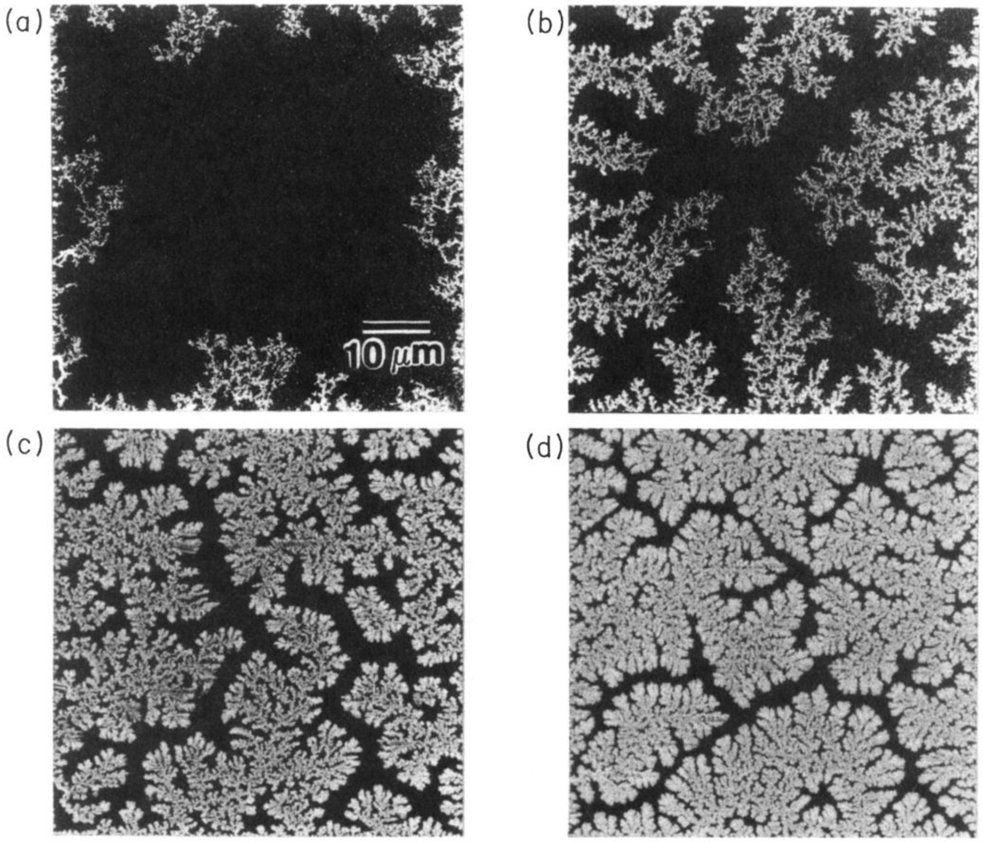

FIG. 1. Gallium oxide growth across cleaned (60 μm)^2 square windows of liquid gallium, imaged with the Ga$^+$ SIMS signal ($P=5.0\times10^{-7}$ Torr, $T=27.7\,^\circ$C). Bright regions correspond to oxide; on the oxide, intensity is related to film thickness. (a) Growth time $t=60$ s, fractional oxide coverage $C(t)/A_0=0.07$, measured dimension $D=1.60$. (b) $t=300$ s, $C(t)/A_0=0.21$, $D=1.68$. (c) $t=1200$ s, $C(t)/A_0=0.51$, $D=1.85$. (d) $t=2400$ s, $C(t)/A_0=0.71$, $D=1.94$. The accuracy of these measurements is discussed in the text.

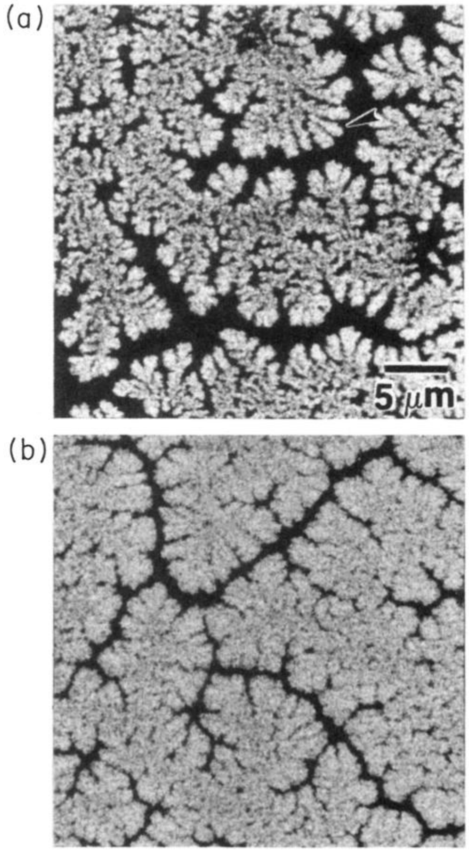

FIG. 9. Oxide growth fronts during late growth ($P=5.0\times10^{-7}$ Torr, $T=27.7\,^{\circ}\mathrm{C}$). Each image is a detail of growth in an $A_0=(80\ \mu\mathrm{m})^2$ window. (a) Growth time $t=2400$ s, fractional oxide coverage $C(t)/A_0=0.67$, measured dimension $D=1.94$. The thicker (brighter) oxide platelet rims are evident. A typical oxide finger within this thick region is indicated. (b) $t=5400$ s, $C(t)/A_0=0.88$, $D=1.99$. Uniform-width gaps in the oxide traverse the growth window.